Optical Materials 131 (2022) 112664

Contents lists available at ScienceDirect

Optical Materials

journal homepage: www.elsevier.com/locate/optmat

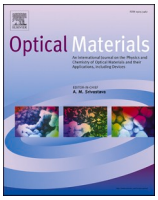

Fabrication of high sensitivity and fast response IR photodetector based on VO_2 nanocrystalline thin films prepared on the silicon substrate

Abbas M. Selman [a,b,*], M.J. Kadhim [c]

[a] Department of Pharmacognosy and Medicinal Plants, Faculty of Pharmacy, University of Kufa, Najaf, Iraq
[b] Institute of Nano Optoelectronics Research and Technology (INOR), Universiti Sains, Malaysia (USM), 11800, Penang, Malaysia
[c] Department of Chemistry, College of Science, University of Basrah, Basrah, Iraq

ARTICLE INFO

Keywords:
VO_2
Nanoparticles
Detectivity
Nanocrystalline
Schottky MSM

ABSTRACT

On Si substrates, vanadium dioxide nanocrystalline thin films (VO_2 NC-TH) were prepared using the radio frequency magnetron sputtering (RF) method. The very small particles reference film was a very thin surface that appeared smooth like a coated Si wafer with the same spherical particle prominent and irregularly distributed in a thin film, according to XRD patterns with narrow peaks intensity and field emission scanning electron microscopy (FESEM) images. The current-voltage characteristic of metal-semiconductor-metal (M-S-M) VO_2 NC-TH infrared photodetectors (IR-PD) in the dark and irradiated with 850 nm light and intensity was (0.17) mW/cm^2. IR-PD exhibits 603, 3567, 10081, and 17751 sensitivity at 2, 3, 4, and 5 bise voltage, with increasing bias voltage increasing quantum efficiency, responsivity, and detectivity. The responsitivity and detectivity under 2, 3, 4, and 5 V bias are (0.24, 1.58, 7.92, and 14.76) A/W and (0.176, 1.03, 3.81 and 6.98) x 10^{12} Jones, respectively.

1. Introduction

Because of their unique physical, chemical, and mechanical properties, nanomaterials have recently attracted a lot of attention. Controlling the size, structural type, and surface states of nanocrystalline materials can be used to influence fundamental attributes of materials such as magnetic, optical, and electrical properties without changing their composition of chemicals [1]. Many nanomaterials have been incorporated into the installation of many devices and applications, such as photocatalysis [2,3], photosensor [4,5], gas sensor [6,7], solar cell [8], subercupastence [9], photodetector [10], etc. Vanadium dioxide (VO_2) has long been regarded as a leading thermochromic material due to its good temperature-responsive behavior at a crucial transition temperature of 68 °C, which is close to room temperature, making it an ideal option for smart architectural glazing [11]. Because its electrical and optical properties can be controlled and tweaked by an external signal, vanadium dioxide (VO_2) is one of the most disruptive options, and its development has been greatly accelerated in recent years [12]. At low temperatures, VO_2 transitions from an infrared-transparent semiconductor state to an infrared-reflective metallic state at high temperatures, while preserving visible transmittance [11]. Below the transition temperature, VO_2 has a monoclinic structure and is insulating, with VO_2 particle pairs having a high band gap of 0.6 eV [13]. The physical properties of VO_2 were shown to be substantially influenced by its morphologies of nanostructured [14] such as nano pourose [15], nanorod [16], nanoparticles [17], etc. Therefore, synthesis was done by many methods, such as hydrothermal [18], chemical bath deposition [19], and RF magnetron sputtering [20]. This study is described as the synthesis of VO_2 nanoparticles deposited onto a P-type Si (100) substrate and a study of its morphology, structure, and optical properties. In addition, using VO_2 NC-TH prepared on a Si substrate for the fabrication of a fast response IR photodetector.

2. Experimental details

The VO_2 nanocrystalline thin films (NC-TH) were generated by radio frequency (RF) reactive magnetron sputtering onto a p-type (100)-oriented silicon wafer for 120 min, with a thickness of around 200 ± 10 nm. The VO_2 disc of high purity (99.99%, 3 in diameter) was employed as a target. The target was pre-sputtered for 5 min before the deposition to clean the target surface. Prior to deposition, the silicon substrate was cleaned with a wet chemical etching utilizing the RCA cleaning procedure outlined in our prior work [21]. The chamber was evacuated below 2 × 10^{-4} mbar with an RF power of 200 W. At a set ratio of 18%,

* Corresponding author. Department of Pharmacognosy and Medicinal Plants, Faculty of Pharmacy, University of Kufa, Najaf, Iraq.,
E-mail addresses: abbasm.salman@uokufa.edu.iq, alabbasiabbas@yahoo.co.uk (A.M. Selman).

https://doi.org/10.1016/j.optmat.2022.112664
Received 19 April 2022; Received in revised form 18 June 2022; Accepted 22 June 2022

high-purity argon is employed as a sputtering gas. The deposition was then completed under a total pressure of 3×10^{-2} mbar. At a deposition rate of 3.6 A/s, the sample was deposited onto a heated substrate at 25 °C. The structure and morphology of the prepared VO_2 NC-TH were characterized and analyzed using high-resolution XRD equipment (PANalytical X'Pert PRO MRD PW3040) with Cu Ka radiation (k = 1.541 Å) and FESEM (Leo Supra 50VP, Carl Zeiss, Germany) equipped with an energy-dispersive X-ray (EDX) system. (AFM) (Dimension edge, Bruker) was used to determine the surface roughness, under non-contact operation mode, and Nano Drive dimension-edge-tapping image-processing software was utilized to acquire two-dimensional AFM images. This image was examined using the NanoScope III program. The thin films were optically measured using a Shimadzu UV–Vis 1800 spectrophotometer at wavelengths ranging from 200 to 2000 nm [4,22].

3. Results and discussion

3.1. Morphological and structural characterizations of VO_2 NC-TH

Fig. 1a and b depicted the FESEM, noting the very small particles of the reference film were on a very thin surface that appeared smooth on the Si wafer. Fig. 2 depicts EDX, which confirms the presence of vanadium and oxygen in the sample while the morphology of the surface was studied. The AFM measure was depicted in Fig. 3 and shows an RMS value of 33.6 nm of VO_2 NC-TH. Otherwise, Tadeo et al. [23] show the value of RMS is 207 nm of VO_2 deposited on quartz.

Fig. 4 depicts the XRD patterns of the prepared VO_2 NC-TH and refers to the scanning Bragg angle that ranged from 20° to 80°. The diffraction peaks were noted at 26.6°, 51.8°, and 62.9° returned to the Si substrate and corresponding plans (200), (321), and (420), respectively, according to JCPDS card No.01-072-1426. However, the four noted diffraction peaks returned VO_2 at 33.8°, 37.9°, 61.8°, and 59.9°, corresponding to plans (130), (210), (151), and (301), respectively. The VO_2 peaks indicated are indexed to the different planes of the orthorhombic crystal system. According to the Debye-Scherer formula, the crystallite size (C. S) calculated high peck of VO_2 is 36.789 nm [22]:

$$C.S = \frac{K\lambda}{\beta cos\theta} \tag{1}$$

where K, β, λ, and θ are the incident Scherer constant, the FWHM diffraction peak, X-ray wavelength, and the angle between the incident beam and crystal plane respectively. The value of C.S (36.789 nm) is consistent with the conclusion that the described surface appears smooth in the FESEM image. Rajeswaran and Umarji [24] reported that the grain size of VO_2 synthesized by chemical vapor deposition is about 200 nm.

3.2. Optical properties

Fig. 5a depicts the reflectance spectrum of the VO_2 NC-TH as measured in the I-R visible range. The inset explains how to use the spectrum to estimate the optical band gap. By fitting the absorption edge of the spectrum using the Kubelka Munk equation [25,26]:

$$(F(r)h\nu)^2 = A(h\nu - E_g) \tag{2}$$

where $F(r)$, A, $h\nu$, and E_g are Kubelka Munk Function, the proportionality constant, photon and band gap energy, respectively. The optical band gap of the orthorhombic VO_2 was estimated to be 0.6 eV as shown in Fig. 5b, which corresponds to the value of 0.6 eV reported for the monoclinic VO_2 [13]. Because of the small energy gap value where I-R photons will be absorbed, the electron will be excited from the valence band into the conduction band, leaving the hole in the valence band. The charge carrier will then be further separated by adding voltage to the interdigital electrode's terminal, resulting in increased current and the formation of a low resistance state. For this reason, the irradiation intensity rises, and more electrons are excited, resulting in a higher photocurrent and reduced resistance. While the electron transport in solid crystals is constantly influenced by the crystal grain boundaries, especially at the nanoscale, it is worth noting [27].

3.3. Device fabrication

The MSM-structured IR-PD device was produced by depositing an Ag grid (100 nm thickness) on top of VO_2 NC-TH using a metal mask. Early studies [28] show the design and dimensions of the shadow mask. The electrodes were deposited by RF reactive magnetron sputtering, wherein the chamber was evacuated below 3×10^{-5} mbar with an RF power of 120 W. High-purity Ar was employed as a sputtering gas at a constant ratio of 17%. The deposition was then done under a total pressure of 3×10^{-3} mbar. The contacts were prepared at room temperature. Fig. 6 depicts a schematic of the device structure. The active area of the (Ag/VO_2 NC-TH/Ag) MSM-structured IR-PD was 0.1634 cm^2 [29,30]. Previous work [28] shows the dimensions, interelectrode spacing, and shadow mask design.

3.4. Current-voltage characteristics

Fig. 7 depicts the I–V characteristics of VO_2 NC-TH MSM IR-PD fabricated under dark and light by 0.17 mW/cm^2 intensity of 850 nm light. The photodetector-produced current was measured with bias voltages ranging from -1V to 3V applied to the contacts. With increasing applied voltage, the photodetector exhibits nonlinear behavior and increases current. The photocurrent is produced when the photodetector is exposed to light, which raises the overall amount of current by forming

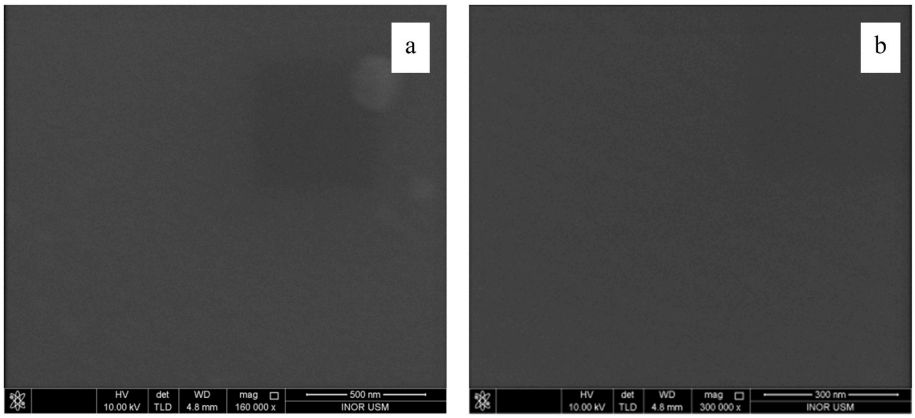

Fig. 1. FESEM images of the VO_2 NC-TH prepared on Si substrate at (a) 500 nm and (b) 300 nm.

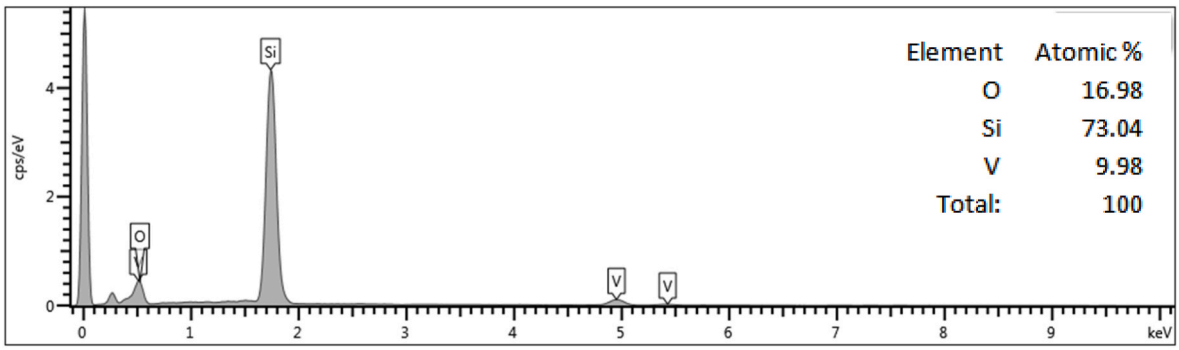

Fig. 2. The EDX spectra results of VO_2 NC-TH prepared on Si substrate.

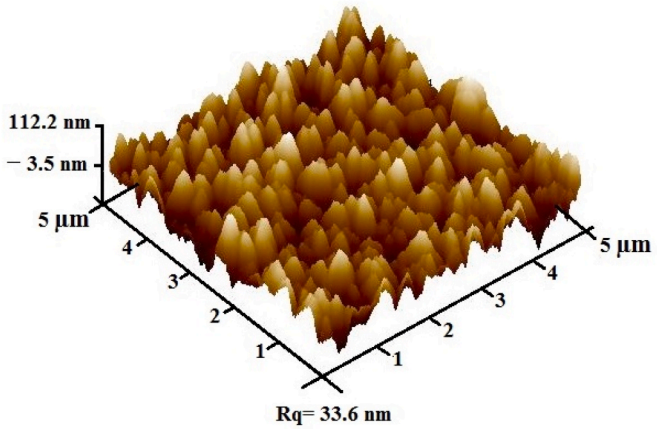

Fig. 3. AFM 3D micrograph of VO_2 NC-TH prepared on Si substrate.

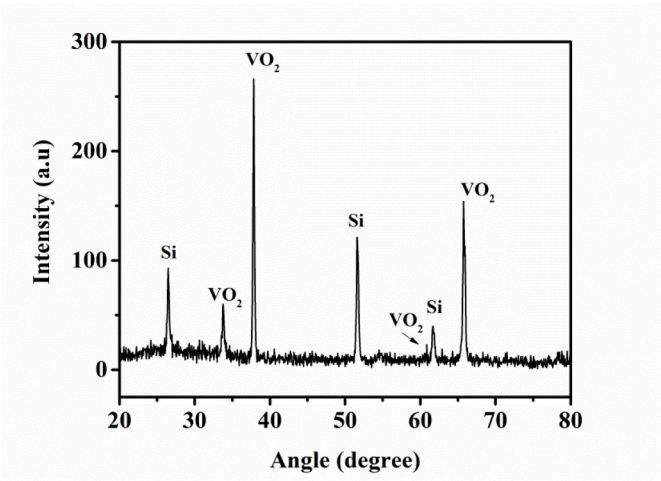

Fig. 4. XRD spectra of VO_2 NC-TH prepared on Si substrate.

charge carrier pairs. Because most detectors are designed to detect a specific wavelength or range of wavelengths, researching the photosensor's photoresponse can assist in determining the sensor's response peak [22]. The applied electric field produces photogenerated charge carrier pairs when the device is illuminated. As a result, the photocurrent generated by the charges added to the bias current effectively increases device conductivity. Also noticed high vlue dark current may be the reason for the combined impacts of residual impurities, surface asperities, and asperities, which have a noticeable influence on electronic contact characteristics, were blamed for the high value of dark current. As a result, the barrier thins out enough for carriers to tunnel through [28,31].

Fig. 8 depicts the response time of VO_2 NC-TH MSM IR-PD and chopped irradiation of 850 nm UV light with 0.17 mW/cm^2 under 2 to 5 bias voltages. It is shown that when the sample was lit, the photocurrent surged to saturation, and when the light was turned off, the photocurrent declined. Consequently, the photodetector's average rise time speed was calculated as about 0.5 ms when increasing the current from 10% to 90% of its value of saturation. In other words, the average fall time is 0.1 ms when the current decreases from 90% to 10% of its value of saturation. The rise time under (2, 3, 4, and 5) V bais is 0.2, 0.4, 0.7, and 0.8 ms, respectively. Over time, fall times under the above bias voltage are 0.12 ms for the 2 V and 0.11 ms for the rest of the bias voltages. The detector's quicker recovery time under 2V was observed in the return data. The photocurrent is produced when the photodetector is exposed to light, which raises the overall amount of current by forming electron-hole pairs. Because most detectors are designed to detect a specific wavelength or range of wavelengths, researching the photosensor's photoresponse can aid in determining the sensor's response peak [22]. Hence, the power-law agrees with the faster reaction and decay times found at increased bias, which can be attributed to efficient charge carrier separation [32]. On the other hand, recombination kinetics are influenced by trap states and interactions between photogenerated charge carriers at reduced bias voltage [33]. The photosensitivity (S) is a parameter that affects how much more photocurrent goes through the photodetector when compared to the dark current. The equation can be used to evaluate the photosensitivity of the produced VO_2 NC-TH MSM IR-PD at various applied biases [34]:

$$S\% = \frac{I_{ph} - I_d}{I_d} \times 100 \tag{3}$$

where I_{ph} and I_d are photocurrents under irradiation and dark, respectively. The photosensitivity of VO_2 NC-TH MSM IR-PD under 2, 3, 4, and 5 V bias is 603%, 3567%, 10081%, and 17751%, respectively. However, responsitivity (R) was evaluated in MSM IR-PD, which is represented by the relation [35]:

$$R = \frac{I_{ph}(A)}{E(w/cm^2)A(cm^2)} \tag{4}$$

where E and A indicate the ratio of photocurrent to incident light power density on the MSM IR-PD effective active area. The responsitivity of VO_2 NC-TH MSM IR-PD under 2, 3, 4, and 5 V bias are (0.24, 1.58, 7.92, and 14.76) A/W, respectively. While Rajeswaran et al. [32] reported R-value is 3.67 × 10^{-2} A/W at a 5 V bias. Quantum efficiency (η) is one of the most important elements in determining a photosensitive device's performance. It is calculated using eq. (4) and is proportional to the number of charge carrier pairs activated by absorbed photons [36]:

$$\eta = \frac{hCR}{e\lambda} \tag{5}$$

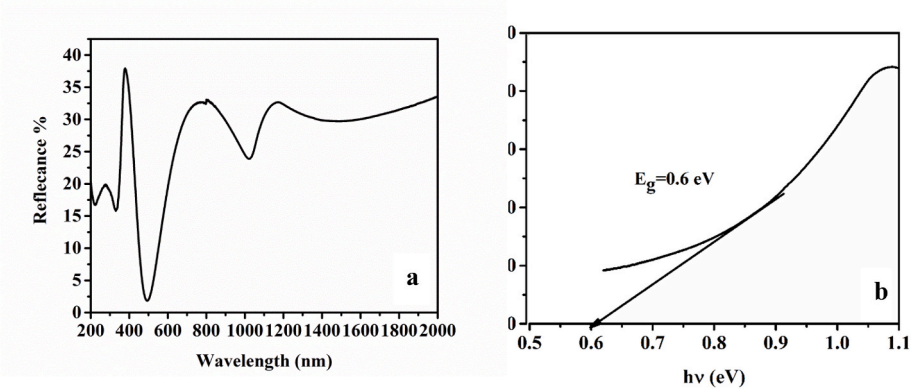

Fig. 5. (a) Reflectance spectrum of VO_2 NC-TH prepared on Si substrate (b) A plot of F(r) $h\nu^2$ versus ($h\nu$).

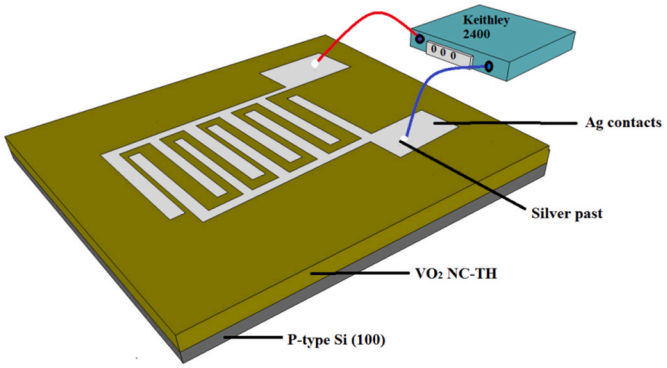

Fig. 6. The schematic diagram of the device (VO_2 NC-TH MSM IR-PD).

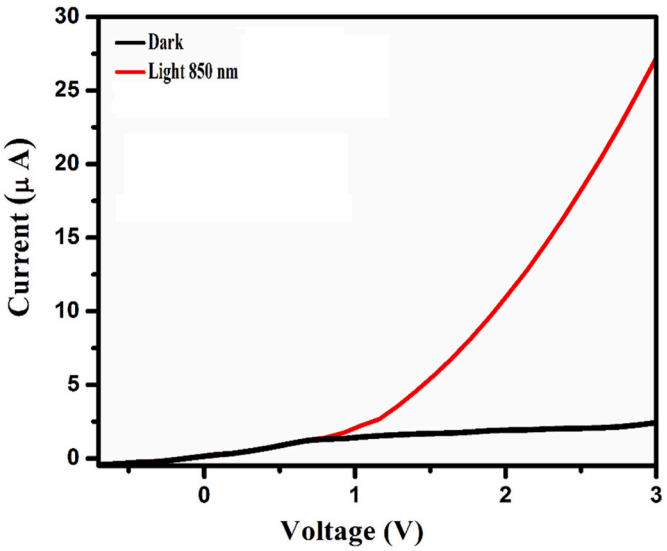

Fig. 7. I–V characteristic of M-S-M VO_2 NC-TH MSM IR-PD in dark and irradiation.

where h, e, c, and λ are the electric charge, Plank's constant, speed of light, and wavelength of IR light, respectively. The quantum efficiency of IR-PD under 2, 3, 4, and 5 V bias is 0.35, 2.31, 11.56, and 21.54, respectively. At a bias voltage of 5 V, the quantum efficiency more than doubled, indicating that charge carriers are separated better at higher voltages. These results are higher than those reported by Jude et al. [33] and Tadeo et al. [23] under 5 and 10 V bias. A photodetector's detectivity (D) is defined as the lowest level at which it may respond, as shown in the following equation [37]:

$$D = \frac{R\sqrt{A}}{\sqrt{2eI_d}} \tag{6}$$

A comparison of the key parameters of PD for the present VO_2 NC-TH MSM IR-PD and other characteristic semiconducting-based VO_2 IR detectors is represented in Table 1. The table noted that the detector in the study has excellent results compared to other researchers, as they obtained high results after modifying the surface or adding another compound that contributed to raising the physical parameters of the detector.

4. Conclusions

VO_2 NC-TH prepared on the Si substrate was synthesized by the RF method. XRD patterns show that the synthesis of thin films is polycrystalline. Hence, the XRD diffraction peaks were noted at 26.6°, 51.8°, and 62.9° returned to the Si substrate and corresponding plans (200), (321), and (420), respectively, according to (JCPDS card No.01-072-1426). However, the four noted diffraction peaks returned VO_2 at 33.8°, 37.9°, 61.8°, and 59.9° corresponding to plans (130), (210), (151), and (301), respectively. On the other hand, the reflectance spectrum of the VO_2 NC-TH as measured in the I-R visible range and the optical band gap of the orthorhombic VO_2 was estimated to be 0.6 eV. The IR-PD appears to result in responsivity increases with increasing voltage bias under 850 nm of irradiation of (0.17) mW/cm^2 light intensity, which indicates results that the VO_2 NC-TH IR-PD shows excellent stability over time, good sensitivity, and high photocurrent, and it is low cost. Therefore VO_2 NC-TH IR-PD on a large scale for use in optoelectronic devices as well as a variety of energy conservation and harvesting applications.

CRediT authorship contribution statement

Abbas M. Selman: Conceptualization, or Conception and design of study, Supervision, and, Project administration, Data curation, or Acquisition of data, Resources, Software, Validation, and, Visualization, Funding acquisition, Investigation, and, Methodology, Formal analysis, and/or interpretation of data: Drafting the manuscript, Writing – original draft, Writing – review & editing, and revising the manuscript critically for important intellectual content. **M.J. Kadhim:** Formal analysis, Data curation, Writing – original draft, Writing – review & editing, and/or interpretation of data: Drafting the manuscript, Writing – original draft, Writing – review & editing, and revising the manuscript critically for important intellectual content.

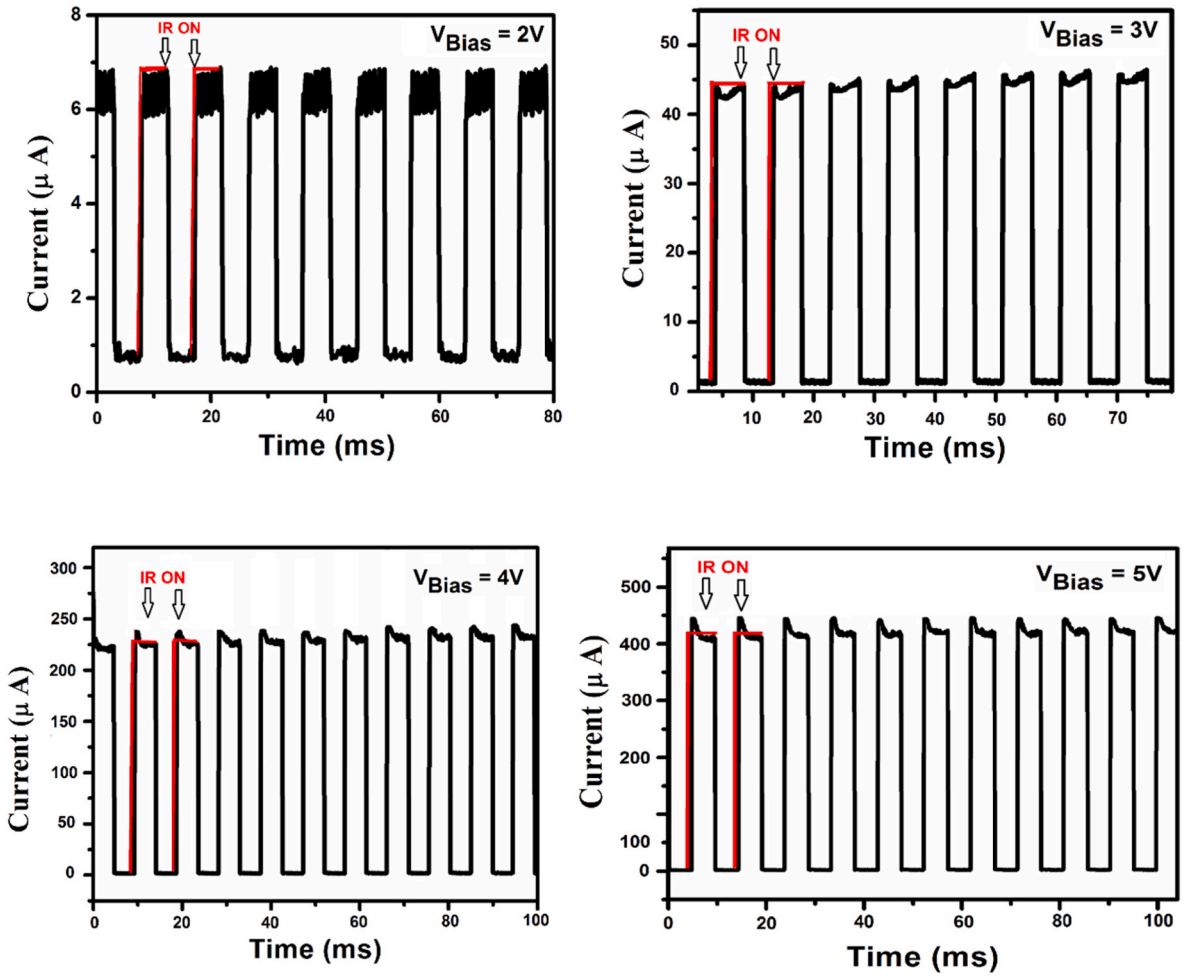

Fig. 8. Response time of M-S-M VO_2 NC-TH MSM IR-PD irradiation by chopped 850 nm of 2, 3, 4, and 5 V bias.

Table 1
Comparison of the key parameters for the present VO_2 NC-TH MSM IR-PD and other characteristic semiconducting based VO_2 IR detectors.

Bias Voltage	Materials	Illumination source	S%	R (A/W)	D (Jones)	η	Ref.
1	Au/VO_2	I-R 808 nm	–	502.1×10^{-3}	1.83×10^{11}	–	[38]
3	n-VO_2/p-GaAs	980 nm	–	0.0025	2.64×10^{10}	–	[39]
0			–	0.013	5.07×10^{9}	–	
3		1310 nm	–	0.0048	4.42×10^{10}	–	
0			–	0.022	9.63×10^{9}	–	
2	VO_2(M)/V_2O_5 core/shell nanobeam heterostructures	990 nm 0.2 mW/cm^2	–	2873.7	9.23×10^{12}	–	[40]
20	H doped VO_2 nanoparticle	780 nm 88 mW/cm^2	–	3.6×10^{4}	1.1×10^{13}	6×10^{6}	[41]
5	VO_2 (M1) thin films	1550 nm 250 mW/cm^2	654.5	3.67×10^{-2}	5.47×10^{10}	2.93×10^{-3}	[32]
10			1272.7	7.13×10^{-2}	1.06×10^{11}	5.71×10^{-3}	
10	VO_2(M1) thin films	1064 nm	–	1.54	3.53×10^{10}	0.18	[23]
5	VO_2(M1) thin films	1064 nm 250 mW/cm^2	–	40.09	7.07×10^{11}	4.67	[33]
2	VO_2 NC-TH MSM IR-PD	850 nm	603	0.241	1.76×10^{11}	0.35	This work
3		0.17 mW/cm^2	3567	1.584	1.03×10^{12}	2.31	This work
4			10081	7.919	3.81×10^{12}	11.56	This work
5			17751	14.759	6.98×10^{12}	21.54	This work

Declaration of competing interest

The authors declare that they have no known competing financial interests or personal relationships that could have appeared to influence the work reported in this paper.

Acknowledgments

The authors would like to thank Prof. Dr. Z. Hassan and all of the technical staff at INOR-Universiti Sains Malaysia for their assistance with this research project.

References

[1] M.A. Mahdi, Z. Hassan, S.S. Ng, J.J. Hassan, S.K.M. Bakhori, Structural and optical properties of nanocrystalline CdS thin films prepared using microwave-assisted chemical bath deposition, Thin Solid Films 520 (9) (2012) 3477–3484, https://doi.org/10.1016/j.tsf.2011.12.059.

[2] M.J. Kadhim, M. Mahdi, J.J.J. Hassan, A.S. Al-Asadi, Photocatalytic activity and photoelectrochemical properties of Ag/ZnO core/shell nanorods under low-intensity white light irradiation, Nanotechnology 32 (2021).

[3] M.J. Kadhim, M.A. Mahdi, J.J. Hassan, Influence of pH on the photocatalytic activity of ZnO nanorods, Mater. Int. 2 (2) (May 2020), https://doi.org/10.1007/s10854-016-4284-0, 0064–0072.

[4] A.M. Selman, M. Husham, Calcination induced phase transformation of TiO2 nanostructures and fabricated a Schottky diode as humidity sensor based on rutile phase, Sens. Bio-Sensing Res. 11 (2016) 8–13, https://doi.org/10.1016/j.sbsr.2016.09.003.

[5] A.A. Abdul-Hameed, et al., Fabrication of a high sensitivity and fast response self-powered photosensor based on a core-shell silicon nanowire homojunction, Superlattice. Microst. 116 (2018) 27–35, https://doi.org/10.1016/j.spmi.2018.02.003.

[6] J.J. Hassan, M.A. Mahdi, C.W. Chin, H. Abu-Hassan, Z. Hassan, Room temperature hydrogen gas sensor based on ZnO nanorod arrays grown on a SiO2/Si substrate via a microwave-assisted chemical solution method, J. Alloys Compd. 546 (2013) 107–111, https://doi.org/10.1016/j.jallcom.2012.08.040.

[7] J.J. Hassan, M.A. Mahdi, C.W. Chin, H. Abu-Hassan, Z. Hassan, Room-temperature hydrogen gas sensor with ZnO nanorod arrays grown on a quartz substrate, Phys. E Low-dimensional Syst. Nanostructures 46 (2012) 254–258, https://doi.org/10.1016/j.physe.2012.08.013.

[8] A.S. Obaid, M.A. Mahdi, Z. Hassan, M. Bououdina, Preparation of chemically deposited thin films of CdS/PbS solar cell, Superlattice. Microst. 52 (4) (2012) 816–823, https://doi.org/10.1016/j.spmi.2012.06.024.

[9] A.S. Al-Asadi, et al., Aligned carbon nanotube/zinc oxide nanowire hybrids as high performance electrodes for supercapacitor applications, J. Appl. Phys. 121 (12) (2017), 124303, https://doi.org/10.1063/1.4979098.

[10] S.M. Saleh Al-Khazali, H.S. Al-Salman, A. Hmood, Low cost flexible ultraviolet photodetector based on ZnO nanorods prepared using chemical bath deposition, Mater. Lett. 277 (2020), 128177, https://doi.org/10.1016/j.matlet.2020.128177.

[11] C. Liu, X. Cao, A. Kamyshny, J.Y. Law, S. Magdassi, Y. Long, VO2/Si-Al gel nanocomposite thermochromic smart foils: largely enhanced luminous transmittance and solar modulation, J. Colloid Interface Sci. 427 (2014) 49–53, https://doi.org/10.1016/j.jcis.2013.11.028.

[12] L. David, S. Diana, F.C. Juan, A.R. Escutia, Ultra-compact electro-absorption VO 2 – Si modulator with TM to TE conversion, J. Opt. 19 (2017), 035401.

[13] D. Jung, U. Kim, W. Cho, Fabrication of pure monoclinic VO 2 nanoporous nanorods via a mild pyrolysis process, Ceram. Int. (July 2017) (2018), https://doi.org/10.1016/j.ceramint.2018.01.130, 0–1.

[14] W. Ning, H. Yizhong, S. Magdassi, D. Mandler, L. Yi, Formation of VO2 zero-dimensional/nanoporous layers with large supercooling effects and enhanced thermochromic properties, RSC Adv. 3 (65) (2013) 7124–7128, https://doi.org/10.1039/c3ra40370j.

[15] R. Basu, Phase-pure VO 2 nanoporous structure for binder-free supercapacitor performances, Sci. Rep. 9 (2019) 1–11, https://doi.org/10.1038/s41598-019-40225-1.

[16] Q. Liu, et al., Revealing mechanism responsible for structural reversibility of single-crystal VO 2 nanorods upon lithiation/delithiation, Nano Energy 36 (2017) 197–205, https://doi.org/10.1016/j.nanoen.2017.04.023.

[17] Y. Choi, D.M. Sim, Y.H. Hur, H.J. Han, Y.S. Jung, Synthesis of colloidal VO2 nanoparticles for thermochromic applications, Sol. Energy Mater. Sol. Cells 176 (November 2016) (2018) 266–272, https://doi.org/10.1016/j.solmat.2017.12.008.

[18] T. V. O. M, S.R. Popuri, M. Miclau, A. Artemenko, C. Labrugere, A. Villesuzanne, Rapid hydrothermal synthesis of VO 2 (B) and its conversion to, Inorg. Chem. 2 (2013) 4780–4785.

[19] A. Tsige, G. Thothadri, D. Mensur, D. Tesfaye, Thermal studies on chemical bath deposited thermochromic VO2 thin film for energy efficient glass windows, Mater. Today Proc. 45 (2020) 6171–6175, https://doi.org/10.1016/j.matpr.2020.10.480, xxxx.

[20] W. Ren, W. Huang, H. Zhu, D. Wang, L.G. Zhu, Q. Shi, Flexible VO2/Mica thin films with excellent phase transition properties fabricated by RF magnetron sputtering, Vacuum 192 (June) (2021), 110407, https://doi.org/10.1016/j.vacuum.2021.110407.

[21] A.M. Selman, Z. Hassan, M. Husham, Structural and photoluminescence studies of rutile TiO2 nanorods prepared by chemical bath deposition method on Si substrates at different pH values, Measurement 56 (2014) 155–162.

[22] A.M. Selman, M.A. Mahdi, Z. Hassan, Fabrication of Cu2O nanocrystalline thin films photosensor prepared by RF sputtering technique, Phys. E Low-Dimensional Syst. Nanostructures 94 (June) (2017) 132–138, https://doi.org/10.1016/j.physe.2017.08.007.

[23] I.J. Tadeo, E.P. Mukhokosi, S.B. Krupanidhi, A.M. Umarji, Low-cost VO2(M1) thin films synthesized by ultrasonic nebulized spray pyrolysis of an aqueous combustion mixture for IR photodetection, RSC Adv. 9 (2019) 9983–9992, https://doi.org/10.1039/c9ra00189a.

[24] B. Rajeswaran, A.M. Umarji, Defect engineering of VO2 thin films synthesized by Chemical Vapor Deposition, Mater. Chem. Phys. 245 (2020), 122230, https://doi.org/10.1016/j.matchemphys.2019.122230.

[25] S. Landi Jr., I.R. Segundo, E. Freitas, M. Vasilevskiy, J. Carneiro, C.J. Tavares, Use and misuse of the Kubelka-Munk function to obtain the band gap energy from diffuse reflectance measurements, Solid State Commun. 341 (2022), 114573.

[26] S.S. Abdullahi, S. Güner, Y. Koseoglu, I.M. Musa, B.I. Adamu, M.I. Abdulhamid, Simple method for the determınatıon of band gap of a nanopowdered sample usıng Kubelka Munk theory, J. Niger. Assoc. Math. Phys. 35 (August) (2016) 241–246 [Online]. Available: https://www.researchgate.net/publication/305810656.

[27] L. Fan, et al., Well-dispersed monoclinic VO2 nanoclusters with uniform size for sensitive near-infrared detection, ACS Appl. Nano Mater. 1 (9) (2018) 5044–5052, https://doi.org/10.1021/acsanm.8b01126.

[28] A.M. Selman, Z. Hassan, Fabrication and characterization of metal-semiconductor-metal ultraviolet photodetector based on rutile TiO2 nanorod, Mater. Res. Bull. 73 (2016) 29–37, https://doi.org/10.1016/j.materresbull.2015.08.013.

[29] A.M. Selman, M.S. Mahdi, Self-biased high sensitivity near-infrared photodetector based on nanocrystalline indium nitride film, Mater. Latters 318 (2022), 132137.

[30] A.M. Selman, M.J. Kadhim, Fabrication of GaN nanocrystalline thin films Schottky metal-semiconductor-metal ultraviolet photodetectors, Optik 265 (2022), 169418, https://doi.org/10.1016/j.ijleo.2022.169418.

[31] A.M. Selman, Z. Hassana, Effects of variations in precursor concentration on the growth of rutile TiO2 nanorods on Si substrate with fabricated fast-response metal-semiconductor-metal UV detector, Opt. Mater. 44 (1) (2015) 37–47, https://doi.org/10.1016/j.optmat.2015.02.028.

[32] B. Rajeswaran, I.J. Tadeo, A.M. Umarji, IR photoresponsive VO2thin films and electrically assisted transition prepared by single-step chemical vapor deposition, J. Mater. Chem. C 8 (36) (2020) 12543–12550, https://doi.org/10.1039/d0tc02785e.

[33] I. Jude, T. Devanshi, B.D. Sheela, S.B. Krupanidhi, A.M. Umarji, Highly photoresponsive VO 2 (M1) thin films synthesized by DC reactive sputtering, J. Mater. Sci. Mater. Electron. 2 (2020), 0123456789, https://doi.org/10.1007/s10854-020-03023-4.

[34] A.M. Selman, Z. Hassan, M. Husham, N.M. Ahmed, A high-sensitivity, fast-response, rapid-recovery p–n heterojunction photodiode based on rutile TiO2 nanorod array on p-Si(1 1 1), Appl. Surf. Sci. jou 305 (2014) 445–452.

[35] A.M. Selman, Z. Hassan, Highly sensitive fast-response UV photodiode fabricated from rutile TiO2 nanorod array on silicon substrate, Sensors Actuators, A Phys. 221 (2015) 15–21, https://doi.org/10.1016/j.sna.2014.10.041.

[36] M.A. Mahdi, J.J. Hassan, N.M. Ahmed, S.S. Ng, Z. Hassan, Growth and characterization of CdS single-crystalline micro-rod photodetector, Superlattice. Microst. 54 (1) (2013) 137–145, https://doi.org/10.1016/j.spmi.2012.11.005.

[37] N. Prakash, et al., Ultrasensitive self-powered large area planar GaN UV-photodetector using reduced graphene oxide electrodes, Appl. Phys. Lett. 109 (24) (2016), 242102, https://doi.org/10.1063/1.4971982.

[38] X. Zhou, et al., Phase-transition-Induced VO2 thin film IR photodetector and threshold switching selector for optical neural network applications, Adv. Electron. Mater. 7 (5) (2021) 1–9, https://doi.org/10.1002/aelm.202001254.

[39] J. Zhou, et al., Electrical and infrared responses of n-VO2/p-GaAs heterojunctions based on VO2 phase transition properties, J. Phys. D Appl. Phys. 53 (31) (2020), https://doi.org/10.1088/1361-6463/ab87c6.

[40] Z. Li, et al., Ultrahigh infrared photoresponse from core-shell single-domain-VO 2/V2O5 heterostructure in nanobeam, Adv. Funct. Mater. 24 (13) (2014) 1821–1830, https://doi.org/10.1002/adfm.201302967.

[41] M.W. Kim, Y.R. Jo, C. Lee, W.J. Moon, J.H. Shim, B.J. Kim, Ultrafast infrared photoresponse from heavily hydrogen-doped vo2 single crystalline nanoparticles, Nano Lett. 20 (4) (2020), https://doi.org/10.1021/acs.nanolett.0c00358. Nano Lett.